APS physics

CHORUS

This is the accepted manuscript made available via CHORUS. The article has been published as:

Laser-induced-fluorescence imaging of a spin-polarized ultracold neutral plasma in a magnetic field

G. M. Gorman, M. K. Warrens, S. J. Bradshaw, and T. C. Killian

Phys. Rev. A **105**, 013108 — Published 19 January 2022

DOI: 10.1103/PhysRevA.105.013108

Laser-Induced-Fluorescence Imaging of a Spin-Polarized Ultracold Neutral Plasma in a Magnetic Field

G.M. Gorman,[1] M.K. Warrens,[1] S.J. Bradshaw,[1] and T.C. Killian[1]

[1] *Rice University, Department of Physics and Astronomy, Houston, Texas, USA*

(Dated: January 7, 2022)

We report Doppler-sensitive laser-induced-fluorescence (LIF) imaging of an ultracold neutral plasma in a magnetic field. Local values of ion density, hydrodynamic fluid velocity, temperature, and spin polarization are obtained using a fluorescence model based on velocity-resolved rate equations (REs) including the transfer of ions between states due to laser coupling and spontaneous emission. The RE approach captures optical pumping of ions into states that are not driven by the LIF excitation laser, and this is validated with experimental data. Combined molecular-dynamics and quantum-trajectories simulations verify that velocity-changing collisions have a negligible impact on the state population evolution for typical experimental conditions. Relative intensities of Zeeman components of the LIF spectra provide clear evidence that the ions are electron-spin-polarized when created by photoionization of magnetically trapped ^{88}Sr atoms. This probe opens many possibilities for studying thermal transport and equilibration of neutral plasmas in overlapping regimes of strong coupling and magnetization.

I. INTRODUCTION

Ultracold neutral plasmas (UCNPs), created by photoionizing laser-cooled atoms near the ionization threshold [1, 2], have ion temperatures $T \sim 1\,\mathrm{K}$ and tunable electron temperatures $T_e = 1 - 1000\,\mathrm{K}$. They provide an excellent platform for studies of fundamental plasma phenomena due to their well controlled initial conditions, precise diagnostics, and the novel plasma regime explored [3]. Ions in UCNPs are typically strongly coupled [4–6], meaning the Coulomb interaction energy of neighboring particles is greater than the average thermal energy, which enables the experimental study of the impact of strong coupling on phenomena such as transport [7, 8] and equilibration [9–15]. Laser-induced fluorescence (LIF) has been a powerful diagnostic for these studies [12, 16].

Most previous work on UCNPs has focused on plasma behavior in the absence of external magnetic fields. However, there has been emerging interest in magnetized and strongly coupled plasmas in general [8, 17–19] and in the ultracold regime in particular [8, 20–22], driven in large part by new experimental capabilities in dusty [23–25] and laser-produced high-energy-density plasmas [26, 27]. The combined effects of magnetization and strong coupling modify collisional and transport phenomena [21, 28, 29] and are challenging to model theoretically. A generalized Boltzmann kinetic theory spanning weak to strong magnetization was recently developed for weakly coupled plasmas [30], but its extension to the strongly coupled regime is still ongoing.

Magnetic confinement of a UCNP created at the null of a biconic cusp, or quadrupole, magnetic field was recently demonstrated [31]. In the presence of non-uniform magnetic fields, the spatially varying Zeeman shifts and quantization axis of the ions complicates the use of LIF. In this work, we describe LIF of ions in a magnetized UCNP and measurement of ion density, temperature, and hydrodynamic fluid velocity. We also observe electron-spin polarization of the ions when the plasma is formed by photoionizing spin-polarized atoms.

Application of LIF [32] is widespread in many types of plasmas because of its power to provide spatially and temporally resolved measurements of the density, velocity, and internal-state distributions of ionic and neutral species and measurement of electric and magnetic fields without perturbing the plasma. For example, LIF can be used to diagnose plasma processing sources [33], high-temperature plasmas such as in fusion research [34–36], and a large assortment of basic plasma configurations such as helicon plasmas [37], magnetron plasmas [38] magnetically confined pure ion plasmas [39], dusty plasmas [40, 41], and UCNPs [12, 16]. Optical tagging enables measurement of transport properties with LIF [42].

LIF in the UCNPs studied here is relatively straightforward because there is only a single ion species, which occupies the ground electronic state in the absence of driving laser fields, and collision energies and densities are low enough to neglect state-changing collisions. This facilitates detailed, quantitative interpretation of experimental data even with complications arising from the magnetic field. Variation of the polarization of the LIF excitation laser provides additional information from which the electron-spin polarization of the ions can be accurately determined. LIF experiments and models typically account for polarization of the excitation laser light and sometimes discriminate polarization of fluorescence, such as to improve measurement of electric and magnetic fields [43] and state populations [44].

II. EXPERIMENTAL DETAILS

To create a UCNP, Sr atoms are first laser-cooled and confined with a magneto-optical trap (MOT) using the $5s^2\,{}^1S_0 - 5s5p\,{}^1P_1$ transition at 461 nm. Atoms popu-

late the metastable $5s5p\,^3P_2$ state throughout the laser cooling process due to a weak decay path: $5s5p\,^1P_1 \rightarrow 5s4d\,^1D_2 \rightarrow 5s5p\,^3P_2$ [45, 46]. Due to their large magnetic moment, low-field-seeking $^3P_2$ atoms ($m_j = +2$) are efficiently trapped in the quadrupole magnetic field of the MOT [45] due to the interaction energy of the atomic magnetic dipole moment $\vec{\mu}$ with the magnetic field $\vec{B} = B'(-\vec{x} + \vec{y}/2 + \vec{z}/2)$, $U = \langle -\vec{\mu} \cdot \vec{B} \rangle = g_j m_J \mu_B B' \sqrt{x^2 + y^2/4 + z^2/4}$. $g_j = 3/2$ is the Lande g-factor for the $^3P_2$ state, μ_B is the Bohr magneton [47], and $B' = 150\,\mathrm{G/cm}$ is the gradient of the magnetic field along the symmetry axis. The quantization axis is chosen to be along the local magnetic field. The atom cloud is small compared to the radius of the coils creating the magnetic field, so a linear approximation of the field profile is sufficient. The spin-polarized $^3P_2$ atoms are then photoionized near threshold with 322 nm photons from a 10-ns pulsed dye laser. The magnetic fields are left on during photoionization and plasma expansion.

The initial plasma density distribution, $n(\vec{r}) = n_0 \exp(-U/k_B T_a)$, follows the density distribution of the magnetically trapped neutral atoms, with plasma radius of $\sim 1\,\mathrm{mm}$. $T_a \approx 3$ mK is the temperature of the neutral atoms. The initial peak density ($n_0 \sim 10^9\,\mathrm{cm}^{-3}$) is controlled by varying the laser-cooling time ($\sim 1\,\mathrm{s}$) to vary the number of trapped atoms.

The initial electron temperature is set by the photoionization laser detuning above threshold and is typically chosen to be sufficiently high so as to avoid three-body recombination into neutral atoms [48] but low enough to ensure predominantly hydrodynamic conditions. For the results presented here, we use $T_e = 20 - 40\,\mathrm{K}$ in order to validate the LIF model under conditions similar to those used to demonstrate magnetic confinement of a UCNP in a biconic cusp field [31]. The ions are created with extremely low kinetic energy, close to that of the precursor neutral atoms, but they possess significant potential energy due to their initially uncorrelated state and undergo a process called disorder-induced heating (DIH) in the first few 100 ns, resulting in ion temperatures $T_i \sim 1\,\mathrm{K}$ [4, 49].

Following photoionization, electron thermal pressure drives plasma expansion on a characteristic hydrodynamic timescale of $\tau_{exp} = \sqrt{m_i \sigma(0)^2 / k_B T_e(0)}$, where $\sigma(0)$ is the initial geometric mean rms plasma size and m_i is the mass of Sr^+ [50]. The outward expansion velocity tends to increase with time and distance from the plasma center at early times, saturating at a characteristic ion velocity $v \approx \sqrt{k_B T_e(0)/m_i}$, but can become more complicated due to plasma waves [50] and magnetic trapping [31], especially at later times. For $\sigma(0) = 1.1\,\mathrm{mm}$ and $T_e = 20\,\mathrm{K}$, $\tau_{exp} = 25\,\mu\mathrm{s}$.

The plasma is probed at an adjustable time after photoionization using LIF on the $5s\,^2S_{1/2} - 5p\,^2P_{1/2}$ transition of Sr^+ at 422 nm. The decay rate from the $^2P_{1/2}$ state to the $^2S_{1/2}$ state is $\gamma = 1.26 \times 10^8\,\mathrm{s}^{-1}$ [51]. The LIF laser, with detuning Δ from unperturbed resonance, illuminates a $w = 1\,\mathrm{mm}$ thick central slice of the plasma

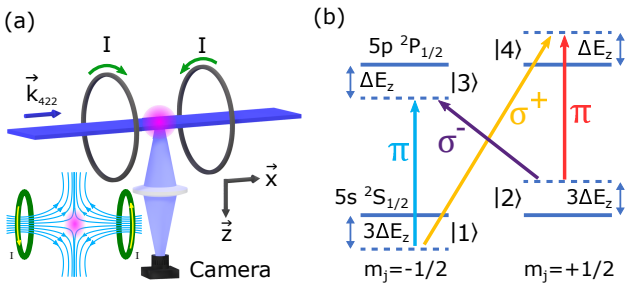

FIG. 1. (a) Experimental schematic for laser-induced-fluorescence (LIF) imaging and application of quadrupole magnetic fields using anti-Helmholtz coils (inset depicts field lines). The plasma is illuminated by a thin sheet of 422-nm light that propagates along the x axis. For data described here, LIF polarization is linearly polarized along the y axis, left-hand circular, or right-hand circular. The ion fluorescence is imaged onto an intensified CCD camera using a 1:1 optical relay along the z axis. (b) Sr levels coupled by LIF laser with (dashed) and without (solid) Zeeman shifts, with quantization axis taken to be along the local magnetic field.

($z \approx 0$) (Fig. 1(a)). A 1:1 optical relay is used to image scattered photons onto an intensified CCD camera over an excitation period with duration $\tau_E = 0.25 - 2\,\mu\mathrm{s}$, set by CCD and LIF laser gating to obtain a spatially resolved LIF fluorescence spectrum, $F(x, y, \Delta)$, with 50 μm resolution.

The LIF laser is a thin sheet of light propagating along the x axis and polarized in the y-z plane of the lab coordinate system (Fig. 1a). The LIF-laser intensity distribution is measured independently and is approximately Gaussian along the y axis with 6 mm $1/e^2$ radius and exponential along the z axis with $1/e^2$ radius $\approx w/2$, which is accounted for in the analysis. In this work, three different LIF-laser polarizations are used: linear along the y axis or left/right-handed circular (LC,RC). Fluorescence perpendicular to the LIF excitation sheet is imaged onto the intensified CCD camera. No polarization filtering is applied to the fluorescence light.

III. LIF MODEL

The LIF signal collected by the camera from an area $\delta x\,\delta y$ centered at position (x, y) arises from a volume element $V \approx \delta x\,\delta y\,w$ centered at $z = 0$. Assuming negligible variation of plasma properties over this volume, the signal during an excitation period of duration τ_E can be written as

$$F(x, y, \Delta) = V\, C_{p\rightarrow s} \int_0^{\tau_E} d\tau \sum_{e,g} n \bar{p}_e \gamma_{eg} \xi_{eg} \qquad (1)$$

where $C_{p\rightarrow s}$ is a photon-to-signal conversion factor for the camera, which is determined by an independent density calibration that relies on the density dependence of

DIH [11]. The sum runs over both magnetic sublevels of the excited ($|e\rangle = |3\rangle, |4\rangle$) and ground ($|g\rangle = |1\rangle, |2\rangle$) states in Fig. 1(b), where $|1\rangle$ and $|3\rangle$ correspond to $m_j = -1/2$. γ_{eg} and ξ_{eg} are the spontaneous emission rate and the fraction of emitted photons relayed onto the camera, respectively, for decay from excited state $|e\rangle$ to ground state $|g\rangle$. ξ_{eg} accounts for the dipole radiation pattern and optical relay collection solid angle. $\gamma_{32} = \gamma_{41} = 2\gamma/3$ and $\gamma_{31} = \gamma_{42} = \gamma/3$.

A main focus of this paper is the calculation of $\bar{p}_e(\tau, \Delta, n, v_{x,hyd}, T_i, P)$, the ensemble-averaged fraction of ions that occupy excited state $|e\rangle$ after an excitation of duration τ with local LIF-laser intensity I and polarization $\hat{\epsilon}$. n, $v_{x,hyd}$, T_i, and P are the local ion density, hydrodynamic fluid velocity along the LIF-laser propagation direction, ion temperature, and electron-spin polarization inside volume V at position $x, y, z = 0$. These quantities vary with position and plasma evolution time t, but for brevity these dependencies are not explicitly indicated. The plasma density, hydrodynamic fluid velocity, and ion temperature are also assumed to be stationary in time during excitation, which is valid because $\tau_E \ll \tau_{exp}$.

At the beginning of the excitation period ($\tau = 0$), the ions occupy the $^2S_{1/2}$ ground manifold ($\bar{p}_1 + \bar{p}_2 = 1$, $\bar{p}_3 = \bar{p}_4 = 0$) with electron-spin polarization $P = \bar{p}_2 - \bar{p}_1$. The ions are assumed to be in local thermal equilibrium with Maxwell-Boltzmann velocity distribution around $v_{x,hyd}$, $G(v_x, v_{x,hyd}, T_i)$, therefore the probability that an ion with velocity v_x occupies state $|k\rangle$ at $\tau = 0$ is given by $p_k(v_x, \tau = 0, n, v_{x,hyd}, T_i, P) = \bar{p}_k(\tau = 0)G(v_x)$. (Here, and going forward, we suppress arguments of functions for clarity.) This formalism only tracks the velocity along the x axis because the Doppler shift of the LIF excitation is only sensitive to this component. For $\tau > 0$, the velocity dependence of $p_k(v_x, \tau)$ is not necessarily Gaussian and the ensemble average can be computed as

$$\bar{p}_k(\tau) = \int_{-\infty}^{\infty} dv_x p_k(v_x, \tau). \tag{2}$$

In the absence of magnetic fields, $F(x, y, \Delta)$ takes on a simple form when imaging a UCNP with linear polarization [16]. In this case, the ion quantization axis is set by the LIF-laser polarization direction, so the degenerate π transitions are driven equally and p_e quickly stabilizes after a few times the excited-state lifetime ($\gamma^{-1} \approx 8$ ns). The resulting spectrum, typically recorded after an excitation period of a few 100 ns, can be described as a single Voigt profile, formed by convolving the single-particle, power-broadened Lorentzian lineshape with the local velocity distribution [16].

In the presence of quadrupole magnetic fields, this simplicity is lost due to Zeeman shifts of the LIF transitions and the varying direction of the magnetic field, which is chosen as the quantization axis (Fig. 1(b)). The laser excitation rate from ground state $|g\rangle$ to excited state $|e\rangle$ is given by

$$R_{eg} = \frac{\Omega_{eg}^2 \gamma_{tot}}{\gamma_{tot}^2 + 4\Delta_{eg}^2}, \tag{3}$$

where Ω_{eg} is the Rabi coupling between the respective states, Δ_{eg} is the Doppler- and Zeeman-shifted resonance condition, and $\gamma_{tot} = \gamma + \gamma_L$ is the effective linewidth including the laser linewidth $\gamma_L/2\pi = 5\,\mathrm{MHz}$. The resonance condition and Rabi couplings that determine the laser excitation rate for each transition are dependent on the spatially varying magnetic field strength and direction, respectively. In order to determine Ω_{eg}, the LIF-laser polarization must be projected onto the coordinate frame of the local magnetic field and then expressed in the spherical tensor basis (App. A). The largest coupling in this work, $\Omega \approx 0.375\gamma$, occurs while imaging with LC/RC polarization with the local magnetic field parallel to the LIF-propagation direction. The observed strength of each spectral Zeeman component depends on the laser polarization and $P(\tau = 0)$.

In Eq. 1, the effects of the magnetic fields, the LIF-laser intensity and polarization, and electron-spin polarization are contained within p_e, which is calculated using the following set of rate equations (REs) that describe the transfer of ion population between states due to photon scatter and spontaneous decay, including decay into the metastable $^2D_{3/2}$ manifold, which occurs with rate $\gamma_D = 9.0 \times 10^6\,\mathrm{s}^{-1}$ [3].

$$\begin{aligned} \frac{\partial p_g}{\partial t} &= \sum_e -R_{eg}(p_g - p_e) + \gamma_{eg} p_e \\ \frac{\partial p_e}{\partial t} &= \sum_g (R_{eg}(p_g - p_e) - \gamma_{eg} p_e) - \gamma_D p_e \end{aligned} \tag{4}$$

The REs are solved using a 4th-order Runge-Kutta method with a fixed timestep $d\tau = 0.25\gamma^{-1}$ for $\tau < 4\gamma^{-1}$ to capture the initial rise and $d\tau = 2\gamma^{-1}$ at later times to capture the longer timescale changes due to optical pumping. The RE formalism neglects the time dependence of ion coherences that are present in an optical Bloch treatment, which is justified because $\gamma^{-1} \ll \tau_E$. This treatment neglects velocity-changing collisions, which is justified using combined molecular-dynamics and quantum-trajectories (MDQT) simulations for typical experimental densities $n = 10^6 - 10^9\,\mathrm{cm}^{-3}$ (App. B). Because transfer between different velocity classes can be neglected, the v_x and Δ dependence of p_e can in practice be reduced to a dependence on the Doppler-shifted laser detuning $\Delta' = \Delta - kv_x$. The REs are solved for $p_e(\Delta', \tau)$ at a distribution of Δ' values and then the solutions are interpolated and convolved with the Maxwell-Boltzmann distribution of detunings to find $\bar{p}_e(\Delta, \tau)$. We also confirm the validity of this approach with a RE formalism that includes collisions through a Bhatnagar–Gross–Krook collision term (App. B).

Equation 1 makes the simplifying approximation of evaluating all quantities at the center of the volume V,

which greatly reduces computational overhead compared to integrating and accounting for the variation of $\vec{B}$ and I across the local volume element. δx and δy are chosen to be sufficiently small such that the spatial variation of all quantities in the x-y plane can be neglected. However, significant variation of I over the camera line of sight along the z axis cannot be avoided. The most important impact of this variation is on the amount of optical pumping. Computationally expensive calculations of spectra were performed, explicitly integrating over the z axis. It was found that the simple calculation (Eq. 1) with an effective laser intensity $\bar{I} = 0.45 I_{max}$ accurately matched the results of the more expensive calculation over a wide range of conditions (Appendix C). This effective value and Eq. 1 were used for all results presented in this paper. The code for the spectrum fit model (Eqs. 1-4) is publicly available [54].

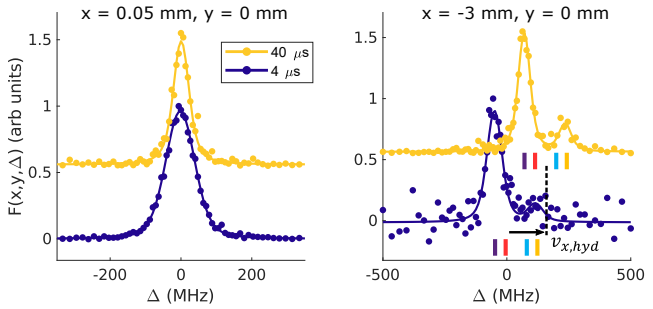

FIG. 2. LIF spectra of regions centered near the field null (left) and at $x = -3\,\text{mm}$, $y = 0\,\text{mm}$ (right) recorded with linear LIF-laser polarization for a UCNP with $T_e(0) = 40\,\text{K}$. The legend indicates time after photoionization and the spectra are normalized to the same amplitude and offset in the vertical scale for clarity. The spectral area scales with plasma density (n). Through the Doppler shift, the hydrodynamic fluid velocity ($v_{x,hyd}$) and ion temperature (T_i) manifest as a mean shift and broadening of the spectrum, respectively. Different Zeeman components are unresolved near the field null (left), but away from plasma center (right) the splitting is resolved. The resonance positions of individual transitions are marked by ticks with color matching the corresponding transitions in Fig. 1(b). Note that the Zeeman splitting is small for transitions initiating from the same ground state. The relative strengths of the resolved Zeeman components are sensitive to the electron-spin polarization of the ions. For this data, the majority of the ions occupy the field-aligned $m_j = +1/2$ ground state at the beginning of the excitation period, and transitions from this initial state are stronger. Polarization persists throughout the expansion. Lines are fits to spectra using Eqs. 1-4.

IV. RESULTS

1. *General Characteristics of LIF Spectra*

Figure 2 demonstrates how the LIF spectra depend on the various plasma parameters for a plasma imaged a short time after photoionization ($t = 4\,\mu\text{s}$), when plasma expansion velocity is still small, and at a later time ($t = 40\,\mu\text{s}$) when the plasma has developed significant expansion velocity in peripheral regions of the plasma. Through the Doppler effect, $v_{x,hyd}$ and T_i manifest as a mean shift and broadening of the single-particle lineshape, respectively, and the amplitude of the spectrum scales with n. The spin polarization P is derived from the relative strength of the Zeeman components associated with each ground state. These parameters are extracted from fits to the spectra with Eqs. 1-4.

At the field null $x \approx y \approx z \approx 0$ (Fig. 2(left)), where the LIF transitions are degenerate and hydrodynamic fluid velocity is small, the spectra are composed of a single spectral feature that is centered at the unperturbed $5s\,^2S_{1/2} - 5p\,^2P_{1/2}$ resonance frequency. The narrowing of the spectrum from $t = 4\,\mu\text{s}$ to $t = 40\,\mu\text{s}$ reflects decreasing ion temperature as the plasma expands, which is expected for adiabatic expansion under predominantly hydrodynamic conditions. In a non-central region along the x axis (Fig. 2(right)), the transitions are Zeeman-shifted according to the local magnetic field strength. For the linear imaging polarization used for this data, the couplings for each σ transition are equal, and the asymmetry in the strength of the different Zeeman components indicates a high degree of spin polarization. Furthermore, at $t = 40\,\mu\text{s}$, the asymmetry is slightly lower, indicating that the ion spin polarization at this location has decreased with time. The fits with Eqs. 1-4 shown in Fig. 2b demonstrate that the polarization has decreased from $P = 0.73 \pm 0.07$ at $t = 4\,\mu\text{s}$ to $P = 0.63 \pm 0.03$ at $t = 40\,\mu\text{s}$. $v_{x,hyd}$ increases with time, as indicated by the larger mean shift of the spectrum at later time.

One important aspect of the RE model is that it accounts for the optical pumping of ions into states that are dark to the LIF laser. Optical pumping occurs when the scattering rate out of the two LIF ground states is unequal or when ions decay into the $^2D_{3/2}$ manifold, resulting in a decrease in the LIF signal collected per unit time during excitation. Differential scattering rates can develop any time the transitions are resolved or when the couplings to the σ transitions differ.

Fig. 3 demonstrates the impact of optical pumping in a magnetically trapped UCNP [31] in a central (left) and non-central (right) region probed $100\,\mu\text{s}$ after plasma creation with linear laser polarization. At the field null, the scattering rate out of each LIF ground state is equal and ions are only lost to the off-resonant $^2D_{3/2}$ manifold, resulting in a 20% decrease of LIF signal per unit time for 2000 ns excitation compared to 250 ns excitation. Far from the field null, the transitions are resolved and the effects of pumping are more significant, with half the signal lost during the same excitation period due to optical pumping between LIF ground states. In both cases, optical pumping is only significant when the LIF laser is near resonance with an optical transition. The solid lines in Fig. 3 are fits to the local spectra. The density extracted from the fits to Eq. 1 for each excitation time in the re-

spective regions agree within 10% when optical pumping is accounted for.

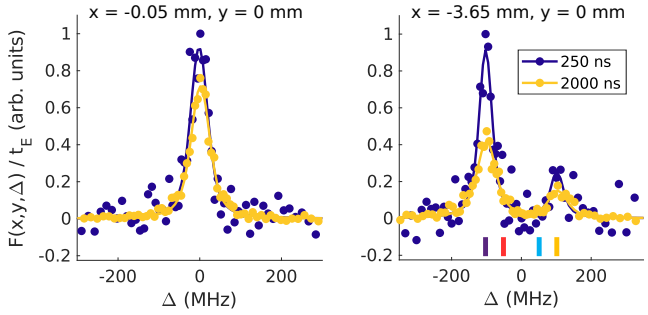

FIG. 3. LIF signal recorded 100 μs after plasma creation with linear laser polarization, illustrating optical pumping of ions into off-resonant states at the field null (left) and far from the field null (right) for a plasma with $T_e(0) = 40$ K. Two different excitation times are used, indicated in the legend, and the signal is divided by the excitation time. Near the field null, where the LIF transitions are degenerate, the signal loss on resonance with increasing excitation time reflects decay of excited ions into the off-resonant $^2D_{3/2}$ manifold. Away from the field null, where the LIF transitions are resolved, the loss of signal on each resonance feature is more severe due to optical pumping into the ground state that is not resonantly excited. Tick marks are the same as in Fig. 2.

2. *Spin Polarization*

Fig. 4 shows measurements of a UCNP after 26 μs of expansion in the biconic cusp field, recorded using LC, linear, and RC polarization (top, middle, and bottom respectively). The 500 ns excitation period is sufficiently small so as to avoid optical pumping. The left column shows a spatial map of the spectral area (integrated over LIF-laser detuning), $F_{int}(x,y) = \int F_R(x,y,\Delta)d\Delta$ for regions (R) with size $\delta x = 0.1$ mm and $\delta y = 0.2$ mm. For linear polarization, the σ transitions are driven equally and the integrated spectra are insensitive to P and the image spatial distribution matches that of the UCNP density distribution. However, for images recorded with LC and RC polarizations, the σ transitions are driven unequally. Imaging light with RC polarization will have a stronger σ^- drive for $x > 0$ and a stronger σ^+ drive for $x < 0$ because the local field direction reflects across the y axis (and vice versa for LC polarization). The asymmetry of the images for circular polarization shows that the ions predominantly occupy the field-aligned Zeeman ground state ($m_j = +1/2$ for quantization axis along the local field).

The right column of Fig. 4 shows $F_R(\Delta)$, the spectrum within a local region R defined by $x = 2.6 \pm 0.1$ mm and $y = 2.07 \pm 0.2$ mm. The solid yellow lines are fits of Eqs. 1-4 to the measured F_R. All three fits in Fig. 4 are constrained to use the same n, T_i, $v_{x,hyd}$, and P fit parameters. The good agreement with the data validates the calculation of Rabi couplings and strongly determines the polarization, which for this region is $P = 0.74 \pm .014$.

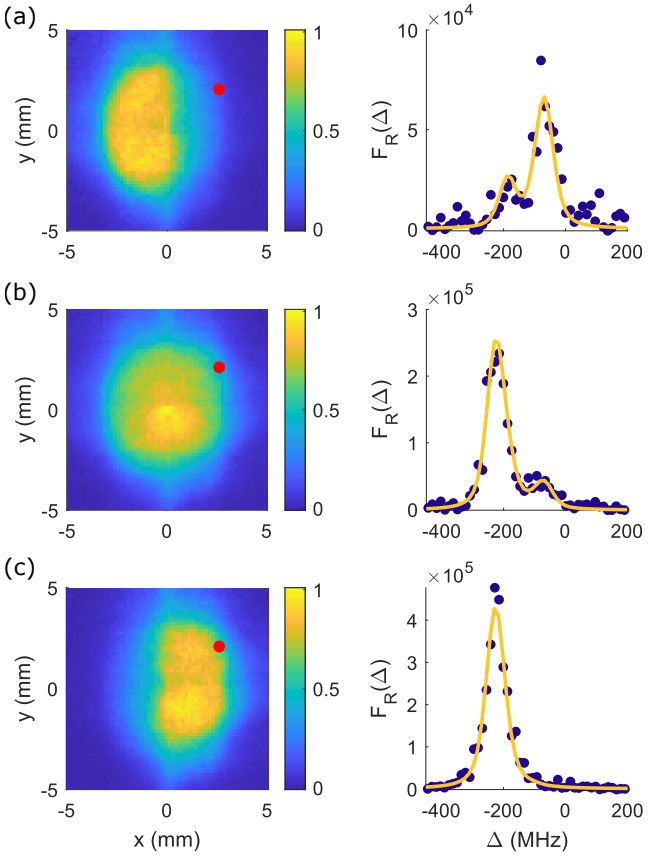

FIG. 4. LIF data for a magnetized UCNP with $T_e(0) = 20$ K recorded at $t = 26$ μs after photoionization with LC (a), linear (b), and RC (c) lab-frame polarization of the imaging laser. The left column shows the integral of the fluorescence spectrum, $\int F_R(x,y,\Delta)d\Delta$, for laser detuning Δ with arbitrary units (the color bars are the same for each image). The image asymmetry along the x axis for LC and RC polarizations occurs because the $\sigma^{\pm}$ transitions are driven unequally, and is therefore reflective of the ion spin polarization. The right column plots the measured LIF spectrum (blue dots) averaged over a region (red circles) defined by $x = 2.6 \pm 0.1$ mm and $y = 2.07 \pm 0.2$ mm, where the magnetic field amplitude is 42 G, as a function of Δ. The data is well described by fits of Eqs. 1-4 (yellow lines), for which n, $v_{x,hyd}$, T_i, and P are constrained to be the same for all three imaging polarizations. The agreement validates the calculation of Rabi couplings for each imaging polarization (see appendix) and demonstrates the plasma is spin polarized.

The spin polarization of the ions is derived from the atomic gas from which the plasma is formed. The $^3P_2$ precursor atoms in the magnetic trap predominantly occupy the $m_j = +2$ magnetic sublevel [45], in which both valence electrons are field-aligned. Following photoionization, the liberated electron carries away the angular momentum of the ionizing photon and the remaining valence electron is unperturbed, such that the ions inherit

the electron-spin polarization from the precursor atoms. The formation of polarized ion targets through photoionization is common for studies of various spin-dependent collision dynamics [52] and can be used for the characterization of magnetic and semiconductor materials [53]. The formation of polarized Sr ions via the photoionization of laser-excited $^3P_1$ Sr atoms has been reported previously [52, 53].

Fig. 5 shows the extracted values of n (left) and P (right) from constrained fits to data such as in Fig. 4 for a plasma after $t = 26\,\mu$s of plasma expansion. The plasma is highly electron-spin-polarized in peripheral regions where the magnetic fields are large, reaching up to $P \approx 0.8$. The spin polarization decreases for ions closer to the field null, which contains a weakly polarized pocket of ions with $P \approx 0.2$ within a 1 mm radius of the field null.

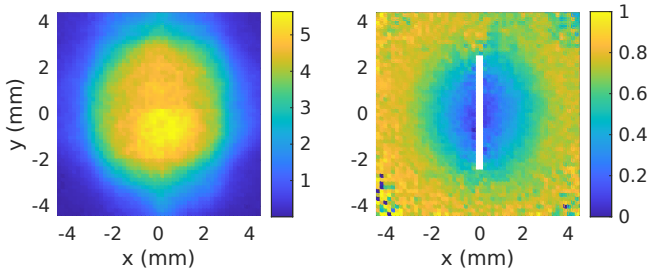

FIG. 5. Measurements of plasma density (n, left) and spin polarization (P, right) for a plasma with $T_e(0) = 20\,$K after $t = 26\,\mu$s$\approx \tau_{exp}$ of plasma expansion, but before the onset of magnetic trapping. The plasma is highly electron-spin-polarized in peripheral regions where the magnetic fields are large, reaching up to $P \approx 0.8$. The spin polarization decreases for ions closer to the field null, which contains a weakly polarized pocket of ions with $P \approx 0.2$ within a 1 mm radius of the field null. The LIF model is insensitive to P within $|x| < 0.15\,$mm and $|y| < 2.5\,$mm for these plasma conditions, so fit results are not shown in these regions. Density is expressed in units of $10^{14}\,\mathrm{m}^{-3}$

The strengths of the Zeeman components depend on the decomposition of the LIF-laser polarization in the coordinate frame of the local magnetic field and the ion spin polarization at the beginning of excitation. These two effects can be decoupled in order to obtain accurate measurements of P anywhere the transitions are resolved or the σ couplings are unequal. However, along the y axis where the transitions are unresolved, neither of these conditions are satisfied for any $\hat{\epsilon}$ and the spectra are insensitive to P. The impact of this issue is mitigated by choosing to define the grid of analysis regions so as to not have regions centered on $x = 0$, although central regions adjacent to the y axis are still more likely to yield poor fit results for P (Fig. 5(right)). For this reason, we do not show fit results for P within $|x| < 0.15\,$mm and $|y| < 2.5\,$mm.

The cause of the gradient in spin polarization is an open question and will be the subject of future study. However, the high degree of polarization away from the plasma center for $t = 26\,\mu$s of plasma expansion implies that the collisional spin-flip rate is low. This suggests that the polarization may provide valuable information for studying plasma flow and diffusion.

V. CONCLUSION

In this work, we described LIF imaging of magnetized UCNPs and a model based on rate equations that describe the population transfer of ions between states involved in LIF due to laser coupling and spontaneous emission. This model can be fit to LIF spectra to extract local measurements of ion density, fluid velocity, temperature, and electron-spin polarization. Observations demonstrate that the ions in a UCNP created by photoionization of magnetically trapped Sr atoms are electron-spin-polarized.

This probe was used in the recent experimental demonstration of magnetic confinement of a UCNP created at the null of a biconic cusp field [31], and it will aid further study of dynamics of magnetized and strongly coupled UCNPs. In future work, we plan to characterize the evolution of ion spin polarization, which could aid in the development of a magnetohydrodynamic model of magnetized UCNP dynamics.

This work was supported by the National Science Foundation(NSF)/Department of Energy Partnership in Basic Plasma Science and Engineering through the NSF Award Number 2107709, the U.S. Air Force Office of Scientific Research through Grant No. FA9550-17-1-0391, and the NSF Graduate Research Fellowship Program under Grant No. 1842494.

[1] T. C. Killian, S. Kulin, S. D. Bergeson, L. A. Orozco, C. Orzel, and S. L. Rolston, Phys. Rev. Lett. **83**, 4776 (1999).
[2] M. Lyon and S. L. Rolston, Rep. Prog. Phys. **80**, 017001 (2017).
[3] T. C. Killian, T. Pattard, T. Pohl, and J. M. Rost, Phys. Rep. **449**, 77 (2007).
[4] C. E. Simien, Y. C. Chen, P. Gupta, S. Laha, Y. N. Martinez, P. G. Mickelson, S. B. Nagel, and T. C. Killian, Phys. Rev. Lett. **92**, 143001 (2004).
[5] M. Lyon, S. D. Bergeson, and M. S. Murillo, Phys. Rev. E. **87**, 033101 (2013).
[6] T. K. Langin, G. M. Gorman, and T. C. Killian, Science **363**, 61 (2019).
[7] T. Strickler, T. Langin, P. McQuillen, J. Daligault, and T. Killian, Phys. Rev. X **6**, 021021 (2016).

[8] S. D. Baalrud and J. Daligault, Phys. Rev. E. **96**, 043202 (2017).

[9] G. Bannasch, J. Castro, P. McQuillen, T. Pohl, and T. C. Killian, Phys. Rev. Lett. **109**, 185008 (2012).

[10] Y. C. Chen, C. E. Simien, S. Laha, P. Gupta, Y. N. Martinez, P. G. Mickelson, S. B. Nagel, and T. C. Killian, Phys. Rev. Lett. **93**, 265003 (2004).

[11] T. K. Langin, T. Strickler, N. Maksimovic, P. McQuillen, T. Pohl, D. Vrinceanu, and T. C. Killian, Phys. Rev. E **93**, 023201 (2016).

[12] E. A. Cummings, J. E. Daily, D. S. Durfee, and S. D. Bergeson, Phys. Rev. Lett. **95**, 235001 (2005).

[13] M. S. Murillo, Phys. Rev. Lett. **96**, 165001 (2006).

[14] T. Pohl, T. Pattard, and J. M. Rost, Phys. Rev. A. **70**, 033416 (2004).

[15] T. Pohl, T. Pattard, and J. M. Rost, Phys. Rev. Lett. **92**, 155003 (2004).

[16] J. Castro, H. Gao, and T. C. Killian, Plasma Phys. Control Fusion **50**, 124011 (2008).

[17] T. Ott and M. Bonitz, Phys. Rev. Lett. **107**, 3 (2011).

[18] S. D. Bergeson, S. D. Baalrud, C. Leland Ellison, E. Grant, F. R. Graziani, T. C. Killian, M. S. Murillo, J. L. Roberts, and L. G. Stanton, Phys. Plasmas **26**, 100501 (2019).

[19] T. Ott, H. Thomsen, J. W. Abraham, T. Dornheim, and M. Bonitz, Eur. Phys. J. D **72**, 84 (2018).

[20] I. L. Isaev and A. P. Gavriliuk, J. Phys. B: At. Mol. Opt. Phys. **51**, 025701 (2018).

[21] S. K. Tiwari and S. D. Baalrud, Phys. Plasmas **25**, 013511 (2018).

[22] J. M. Guthrie and J. L. Roberts, Phys. Plasmas **28**, 052101 (2021).

[23] E. Thomas, R. L. Merlino, and M. Rosenberg, Plasma Phys. Control Fusion **54**, 124034 (2012).

[24] V. Y. Karasev, E. S. Dzlieva, L. G. D'yachkov, L. A. Novikov, S. I. Pavlov, and S. A. Tarasov, Cont. Plasma Phys. **59**, e201800136 (2019).

[25] Y. Feng, S. Lu, K. Wang, W. Lin, and D. Huang, Rev. Mod. Phys. **3**, 10 (2019).

[26] Y. Shi, H. Qin, and N. J. Fisch, Phys. Plasmas **25**, 055706 (2018).

[27] J. J. Santos, M. Bailly-Grandvaux, M. Ehret, A. V. Arefiev, D. Batani, F. N. Beg, A. Calisti, S. Ferri, R. Florido, P. Forestier-Colleoni, S. Fujioka, M. A. Gigosos, L. Giuffrida, L. Gremillet, J. J. Honrubia, S. Kojima, P. Korneev, K. F. F. Law, J.-R. Marquès, A. Morace, C. Mossé, O. Peyrusse, S. Rose, M. Roth, S. Sakata, G. Schaumann, F. Suzuki-Vidal, V. T. Tikhonchuk, T. Toncian, N. Woolsey, and Z. Zhang, Phys. Plasmas **25**, 056705 (2018).

[28] D. J. Bernstein, T. Lafleur, J. Daligault, and S. D. Baalrud, Phys. Rev. E **102**, 041201 (2020).

[29] K. R. Vidal and S. D. Baalrud, Phys. Plasmas **28**, 042103 (2021), publisher: American Institute of Physics.

[30] L. Jose and S. D. Baalrud, Phys. Plasmas **27**, 112101 (2020).

[31] G. M. Gorman, M. K. Warrens, S. J. Bradshaw, and T. C. Killian, Phys. Rev. Lett. **126**, 085002 (2021).

[32] R. A. Stern and J. A. Johnson, Phys. Rev. Lett. **34**, 1548 (1975).

[33] R. McWilliams and D. Edrich, Thin Solid Films Proceedings of the Joint International Plasma Symposium of the 6th APCPST, the 15th SPSM and the 11th Kapra Symposia, **435**, 1 (2003).

[34] R. M. Magee, M. E. Galante, D. McCarren, E. E. Scime, R. L. Boivin, N. H. Brooks, R. J. Groebner, D. N. Hill, and G. D. Porter, Review of Scientific Instruments **83**, 10D701 (2012).

[35] M. Krychowiak, P. Mertens, R. König, B. Schweer, S. Brezinsek, O. Schmitz, M. Brix, U. Samm, and T. Klinger, Plasma Phys. Control. Fusion **50**, 065015 (2008).

[36] K. Muraoka and M. Maeda, Plasma Phys. Control. Fusion **35**, 633 (1993).

[37] R. F. Boivin and E. E. Scime, Review of Scientific Instruments **74**, 4352 (2003).

[38] M. J. Goeckner, J. Goree, and T. E. Sheridan, Journal of Vacuum Science & Technology A: Vacuum, Surfaces, and Films **8**, 3920 (1990).

[39] F. Anderegg, X.-P. Huang, E. Sarid, and C. F. Driscoll, Review of Scientific Instruments **68**, 2367 (1997).

[40] R. S. Marshall and P. M. Bellan, Review of Scientific Instruments **91**, 063504 (2020).

[41] T. Miksch and A. Melzer, Phys. Rev. E **75**, 016404 (2007).

[42] D. A. Edrich, R. McWilliams, and N. S. Wolf, Review of Scientific Instruments **67**, 2812 (1996).

[43] M. Watanabe, K. Takiyama, and T. Oda, Review of Scientific Instruments **70**, 903 (1999).

[44] R. Bergert, L. W. Isberner, S. Mitic, and M. H. Thoma, Phys. Plasmas **28**, 013301 (2021).

[45] S. B. Nagel, C. E. Simien, S. Laha, P. Gupta, V. S. Ashoka, and T. C. Killian, Phys. Rev. A. **67**, 011401(R) (2003).

[46] A. Cooper, J. P. Covey, I. S. Madjarov, S. G. Porsev, M. S. Safronova, and M. Endres, Phys. Rev. X **8**, 041055 (2018).

[47] E. Tiesinga, P. J. Mohr, D. B. Newell, and B. N. Taylor, Rev. Mod. Phys. **93**, 025010 (2021).

[48] R. S. Fletcher, X. L. Zhang, and S. L. Rolston, Phys. Rev. Lett. **99**, 145001 (2007).

[49] M. S. Murillo, Phys. Rev. Lett. **87**, 115003 (2001).

[50] M. K. Warrens, G. M. Gorman, S. J. Bradshaw, and T. C. Killian, Phys. Plasmas **28**, 022110 (2021).

[51] J. E. Sansonetti, Journal of Physical and Chemical Reference Data **41**, 013102 (2012).

[52] T. Nakajima and N. Yonekura, The Journal of Chemical Physics **117**, 2112 (2002).

[53] N. Yonekura, T. Nakajima, Y. Matsuo, T. Kobayashi, and Y. Fukuyama, The Journal of Chemical Physics **120**, 1806 (2004).

[54] G. M. Gorman and T. C. Killian, (2021, December 20), KillianRice/plasma-spectrum-model: LIF of Magnetized UCNP (Version v1.0), Zenodo, http://doi.org/10.5281/zenodo.5792367.

[55] B. E. King, arXiv:0804.4528 [physics] (2008), arXiv: 0804.4528.

[56] R. C. Hilborn, Am. J. Phys. **50**, 982 (1982).

[57] R. Lucht, Prog. Energy Combust. Sci. **29**, 115 (2003).

[58] G. M. Gorman, T. K. Langin, M. K. Warrens, D. Vrinceanu, and T. C. Killian, Phys. Rev. A **101**, 012710 (2020), publisher: American Physical Society.

[59] G. Dimonte and J. Daligault, Phys. Rev. Lett. **101**, 135001 (2008).

Appendix A: Electric Dipole Interaction

For ions with velocity v_x, the interaction with the light field of the imaging laser is described with the Hamiltonian

$$\hat{H}_d = -\frac{\hbar}{2}\left[\hat{\Omega}e^{i(kx-(\nu-kv_x)t)} + c.c.\right], \tag{A1}$$

where $\hat{\Omega} = \frac{eE_0(y,z)}{\hbar}\hat{r}\cdot\hat{\epsilon}(\eta,\xi)$. The amplitude and complex polarization of the LIF laser are $E_0(y,z)$ and $\hat{\epsilon}(\eta,\xi) = \eta\hat{y}+e^{i\xi}\sqrt{1-\eta^2}\hat{z}$, parameterized by $\eta\in[0,1]$ and a phase shift ξ. This work uses three different LIF-laser polarizations: linear polarization along the y axis ($\eta = 1$) or left/right-handed circular polarization (LC,RC: $\eta = 1/\sqrt{2}$, $\xi = \pm\pi/2$). ν is the laser frequency, $k = 2\pi/\lambda$ is the corresponding wavenumber, and c.c. indicates the complex conjugate of the first term.

The Rabi frequency for coupling between lower state $|l\rangle$ and upper state $|u\rangle$ in the fine-structure basis can be expressed as

$$\langle u|\hat{\Omega}|l\rangle = \Omega_{ul} = \Omega_0\epsilon_q^\star(-1)^{j_u+j_l+j_>-m_u}J_{ul}\sqrt{2j_u+1}, \tag{A2}$$

where $\Omega_0 = \sqrt{6\pi\gamma c^2 I/\hbar\omega^3}$, $\omega = ck$, $\gamma = 1.26\times10^8\,\mathrm{s}^{-1}$ is the decay rate from the $^2P_{1/2}$ state to the $^2S_{1/2}$ state, J_{ul} is the 3-j symbol for the transition, j_s is the total angular momentum quantum number for state s, and ϵ_q is the spherical tensor component of the LIF-laser polarization corresponding to $q = m_j^u - m_j^l$, where $m_j^{u/l}$ are the magnetic quantum numbers with the quantization axis aligned along the local magnetic field [55–57]. $j_>$ is the greater of j_u and j_l. The laser intensity is $I(y,z) = \frac{1}{2}c\epsilon_0\left|E_0(y,z)\right|^2$.

The components ϵ_q depend on the direction of the ion quantization axis, which is set by the local quadrupole magnetic field $\vec{B} = B'(-\vec{x}+\vec{y}/2+\vec{z}/2)$, where $B' = 150\,\mathrm{G/cm}$ is the linear magnetic field gradient along the symmetry (x) axis of the anti-Helmholtz coils. The local field coordinate system, denoted by primes, is defined such that $\hat{y}'$ lies in the x-y plane and $\hat{z}' = \hat{B}$. The direction of the local field can be characterized by $\phi = \sin^{-1}(z/\sqrt{4x^2+y^2})$, the angle that $\hat{B}$ subtends from the x-y plane, and $\theta = \tan^{-1}(2x/y)$, the angle that the projection of $\hat{B}$ in the x-y plane subtends with the y axis.

For the results presented here, when applying the spectrum fit model (Eqs. 1-4) the LIF polarization is assumed to lie in the x-y plane ($z = 0$). In this simplifying case, $\phi = 0$ and the expression for $\hat{\epsilon}$ in the local field coordinate system reduces to

$$\hat{\epsilon}(\theta,\phi=0;\eta,\xi) = \sqrt{1-\eta^2}e^{i\xi}\hat{x}' + \eta\sin\theta\hat{y}' + \eta\cos\theta\hat{z}'. \tag{A3}$$

The spherical tensor components of $\hat{\epsilon}$ are obtained by projection onto the spherical basis ($\hat{e}_o = \hat{z}'$ and $\hat{e}_{\pm1} = \mp(\hat{x}'\pm i\hat{y}')/\sqrt{2}$):

$$\epsilon_0 = \eta\cos\theta, \tag{A4}$$

$$\epsilon_{\pm1}(\eta,\xi,\theta) = -\frac{1}{\sqrt{2}}\left[i\eta\sin\theta \pm e^{i\xi}\sqrt{1-\eta^2}\right]. \tag{A5}$$

Appendix B: Collisional Effects in LIF Imaging

Rapid velocity-changing collisions are a hallmark of UCNPs and strongly coupled plasmas in general [9, 58], and can become important in LIF when the velocity dependence of $p_k(v_x,\tau)$ becomes non-Maxwellian. This typically occurs when the Doppler width $\sigma_D = k\sqrt{k_BT_i/m_i}$ exceeds the spectral resolution, γ_{tot}, and the imaging laser optically pumps the resonant portion of the velocity distribution into an off-resonant state. Collisions will cause the velocity distribution to equilibrate to a Maxwellian throughout LIF, effectively increasing the measured signal by providing optical access to the nominally off-resonant portion of the velocity distribution.

The effects of collisions on LIF were quantified by adapting the combined molecular-dynamics and quantum-trajectories (MDQT) code described in [58], which was used to simulate collisional effects during laser cooling of the ions in a UCNP, to simulate LIF of a magnetized UCNP. The MD portion of the code is a particle-in-cell method that evolves the positions and velocities of particles interacting via the Yukawa force. The QT portion of the code evolves the wave function $|\psi(t)\rangle$ for each particle under the influence of an effective, non-Hermitian Hamiltonian that includes the coupling of the ions to the LIF-laser electric field (App. A), the anomalous Zeeman shift, and spontaneous emission from the $^2P_{1/2}$ excited state into the $^2S_{1/2}$ ground state and the $^2D_{3/2}$ dark state. The Hamiltonian is formed in the fine-structure basis from the four magnetic sublevels coupled by the LIF laser (Fig. 1b) and a fifth off-resonant state that grafts on the decay from the excited sublevels into the $^2D_{3/2}$ manifold with rate $\gamma_D = 9.0\times10^6\,\mathrm{s}^{-1}$.

The MDQT simulations of $\bar{p}_k(\tau)$, computed as the ensemble-averaged diagonal elements of the density matrix $\rho(\tau) = |\psi(\tau)\rangle\langle\psi(\tau)|$, were found to be in good agreement with the REs in Eq. 4 modified to include a Bhatnagar–Gross–Krook collision term (Fig. 6)

$$\frac{\partial\rho_k(v_x,\tau)}{\partial t} = -\mu(p_k(v_x,\tau) - \bar{p}_k(\tau)G(v_x)), \tag{B1}$$

which describes the equilibration of $p_k(v_x,t)$ towards a Maxwellian with collisional relaxation rate μ, which is extracted from MD simulations in [59] that were experimentally verified for strongly coupled plasmas in [9]. The value of μ depends on the plasma density (n) and ion temperature (T_i). For a plasma with $T_i = 1\,\mathrm{K}$, the ion-ion collision rate is $\mu = 5.2\times10^4\,\mathrm{s}^{-1}$ for $n = 10^7\,\mathrm{cm}^{-3}$ and $\mu = 1.94\times10^7\,\mathrm{s}^{-1}$ for $n = 10^{11}\,\mathrm{cm}^{-3}$.

Fig. 6 compares MDQT simulations of the instantaneous fluorescence signal per unit density and unit time

(dF/dt) with predictions from the collisional RE (REK) model as a function of plasma density (indicated in the legend) for a plasma with $T_i = 1\,\mathrm{K}$ in a magnetic field of 15 G that is imaged with $I = 100\,\mathrm{W/m^2}$ on resonance with the π transition out of state $|2\rangle$. At early excitation times ($\tau < 100\,\mathrm{ns}$), optical pumping is negligible and there is no density dependence. At later times during excitation, collisional effects manifest as an enhanced fluorescence signal compared to the collisionless model ($n = 0$) for higher plasma densities. For typical experimental densities ($n = 10^6 - 10^9\,\mathrm{cm^{-3}}$), the time-integrated fluorescence signal for $\tau < 500\,\mathrm{ns}$ are within 5% whether or not collisions are included, justifying the use of a collisionless fluorescence model (Eq. 4).

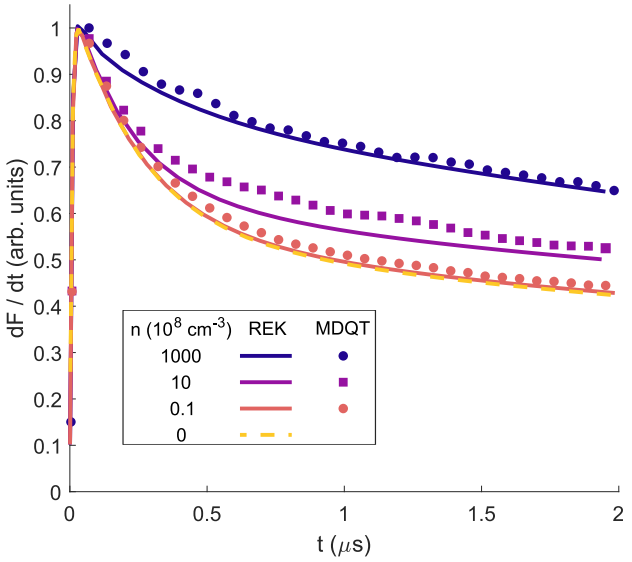

FIG. 6. Effect of collisions on instantaneous fluorescence signal per unit density and unit time (dF/dt) as a function of time during LIF (τ) for a plasma with ion temperature $T_i = 1\,\mathrm{K}$ in a magnetic field of 15 G. Under these conditions, the width of the velocity distribution is broader than the excitation rate. The MDQT simulations (markers) and solutions to the collisional rate equations (REK, lines) are in good agreement. For $\tau < 100$ ns, optical pumping has yet to occur and there is no density dependence. At later times, collisional effects provide optical access to the nominally off-resonant portion of the velocity distribution and manifest as an enhancement of the fluorescence signal. The legend indicates the plasma density, n.

Appendix C: Justifying the Use of an Effective LIF-Laser Intensity

The LIF spectrum model given by Eq. 1 computes the spectrum within a volume element $V \approx \delta x \delta y w$, where $A = \delta x \delta y$ is a user-defined analysis area within the x-y plane and w is the $1/e^2$ diameter of the LIF-laser along the z axis. Eq. 1 makes the simplifying approximation of evaluating all quantities except for the LIF-laser intensity at the center of the volume V in order to avoid the significant computational overhead that spatial integration would impose in order to account for variation of $\vec{B}$ and I across the local volume element. A is chosen to be sufficiently small such that variation of quantities within the x-y plane can be neglected. However, the imaging process inherently averages over the camera line of sight and significant variation of I along the z axis cannot be avoided. The most significant impact of this averaging is in the amount of optical pumping the model predicts. In order to account for this variation, Eq. 1 uses an effective laser intensity $\bar{I} = 0.45 I_{max}$ that is chosen to minimize discrepancy between Eq. 1 and the following realistic model that integrates over the camera line of sight.

$$F(x,y,\Delta) = A\,C'_{p\to s}\int_0^{\tau_E} d\tau \int_{-\infty}^{\infty} dz \sum_{e,g} n\bar{p}_e(z)\gamma_{eg}\xi_{eg}, \tag{C1}$$

where $p_e(z)$ is explicitly stated as a function of z in order to emphasize that the variation of I and $\vec{B}$ are accounted for. The photon-to-signal conversion factor in Eq. C1 is denoted with a prime to differentiate it from that of Eq. 1. The photon-to-signal conversion factors in Eq. C1 ($C'_{p\to s}$) and Eq. 1 ($C_{p\to s}$) are chosen to match predictions of these calculations to experimentally observed signal levels at small exposure time and with no external magnetic fields so as to avoid the effects of optical pumping. The density assumed for this procedure is determined by a density calibration that relies on the density dependence of DIH [11]. $C_{p\to s}$ and $C'_{p\to s}$ differ because the two equations calculate the volume contributing to the signal differently.

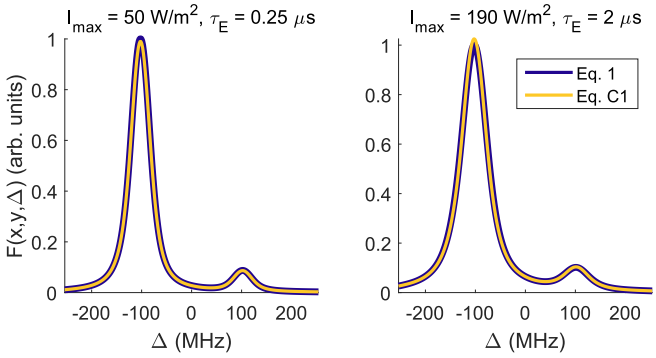

FIG. 7. Comparison of the LIF models given by Eq. 1 (assumes $z = 0$ with an effective LIF-laser intensity) and Eq. C1 (realistic model with spatial averaging) under excitation conditions where optical pumping is minimal (left) and significant (right) for the same spatial region and ion temperature (300 mK) as in Fig. 3b. The two models are in good agreement for both excitation conditions and the relative error in the peak signal is less than 2.5%. The blue line is slightly thicker in order to improve visiblity.

Fig. 7 compares Eqs. 1 and C1 for excitation conditions where optical pumping is minimal (left) and significant (right) for the same spatial region and ion tempera-

ture (300 mK) as in Fig. 3b. $I_{max} = 50\,\mathrm{W/m^2}$ is typical for the edges of the CCD camera near $|y| \approx 5\,\mathrm{mm}$ and $I_{max} = 190\,\mathrm{W/m^2}$ is the maximum intensity used in this work. The models are found to be in good agreement for both excitation conditions with relative error less than 2.5%. In the absence of optical pumping, the agreement is expected and is independent of the choice of $\bar{I}$ due to the external density calibration. $\bar{I}$ is chosen to minimize the difference between the two models when optical pumping is significant. For a given value of $\bar{I}$, the discrepancy between the two models will vary slightly with ion temperature because as the temperature increases the ensemble-averaged scattering rate decreases slightly. The variation with temperature is greatest when optical pumping is significant. For the conditions of greatest optical pumping in this work (Fig. 7(right) and Fig. 3b) and the chosen value of $\bar{I}$, the discrepancy between the two models varies from 0.92% at $T_i = 1\,\mathrm{K}$ to 4.37% at $T_i = 100\,\mathrm{mK}$. Across the relevant parameter regime for this experiment, the discrepancy does not exceed 5% and is typically less than 2.5%.